

# Dynamical Mean-Field Theory for spin-dependent electron transport in spin-valve devices

Andrea Droghetti,<sup>1,\*</sup> Miloš M. Radonjić,<sup>2</sup> Liviu Chioncel,<sup>3</sup> and Ivan Rungger<sup>4</sup>

<sup>1</sup>*School of Physics and CRANN, Trinity College, Dublin 2, Ireland*

<sup>2</sup>*Institute of Physics Belgrade, University of Belgrade, Pregrevica 118, 11080 Belgrade, Serbia*

<sup>3</sup>*Theoretical Physics III, Center for Electronic Correlations and Magnetism,*

*Institute of Physics, University of Augsburg, 86135 Augsburg, Germany*

<sup>4</sup>*National Physical Laboratory, Hampton Road, Teddington TW11 0LW, United Kingdom*

We present the computational implementation of a combination of Density Functional Theory (DFT) and Dynamical Mean Field Theory (DMFT) for studying the linear-response transport properties of two-terminal nanoscale devices. The spin-dependent conductance is determined by the electron transmission through the device region, expressed in terms of the non-equilibrium Green's functions. The developed method is applied to metallic junctions presenting alternating Cu and Co layers, and which exhibit spin-dependent charge transport and giant magnetoresistance (GMR) effect. The calculations show that for energies below the Fermi level the coherent transmission of  $d$  electrons is greatly suppressed by electron correlations. This is mainly due to the finite lifetime induced by the electron-electron correlations on the Co  $d$  orbitals, and it is directly related to the imaginary part of the computed many-body DMFT self-energy. For energies above the Fermi level the transmission is reduced significantly less, since it is mostly determined by  $s$  electrons. At the Fermi energy, in accordance with the Fermi-liquid behaviour, the imaginary part of the self-energy vanishes, and hence the reduction of the transmission predicted by DMFT is entirely due to the shifts of the energy spectrum induced by the electron correlations. The resulting change in transmission and GMR is only moderate. Since this small change of the linear response conductance is due to the inherent Fermi liquid nature of studied systems, we expect that the finding of small changes induced by electron correlations to be a general property of such systems.

## I. INTRODUCTION

Spintronics<sup>1</sup> employs the electron spin for sensing and information technology applications. The prototypical spintronic device is the spin-valve, consisting of two or more conducting ferromagnetic layers - typically  $3d$  transition metals (TMs), whose electrical resistance changes depending the relative alignment of layers' magnetization<sup>2,3</sup>. This phenomenon is called giant magnetoresistance (GMR) effect, and is exploited in the read-heads of hard-disk drives. The GMR is due to the different conductance of the majority and of the minority electrons in ferromagnets. The earlier GMR experiments<sup>4,5</sup> were conducted with the so-called "current-in-plane" configuration, whereas recent experiments use thin film heterostructures, where the current flows perpendicular to the various layers' planes, achieving higher performances<sup>6</sup>.

Over the last decade, there has been considerable progress in the computational modeling of current-perpendicular-to-plane spin-valves. In particular, the ballistic transport properties have been addressed by using the Landauer-Büttiker formalism<sup>7-9</sup>, where the conductance is determined by the electron transmission through the device region, which is placed between two semi-infinite electrodes. The transmission is calculated via the tight-binding approach<sup>10,11</sup> or, in first-principles studies, via density functional theory (DFT)<sup>12-14</sup> within the local spin density approximation (LSDA)<sup>15,16</sup> or the generalized gradient approximation (GGA)<sup>17-19</sup>. Various implementations exist, based

on transfer matrix<sup>20-22</sup>, layer-Korringa-Kohn-Rostoker (KKR)<sup>23</sup>, mode-matching<sup>24</sup> or non-equilibrium Green's function (NEGF) techniques<sup>25-28</sup>. The main assumption underlying the use of DFT is that the effective Kohn-Sham single-particle band structure accurately describes the system's quasi-particle spectral properties. This does however not hold for ferromagnetic  $3d$  transition metals used in spin-valves, since they are moderately correlated<sup>29</sup>. DFT is insufficient for describing their excitation spectra at a quantitative level<sup>30,31</sup>. As a consequence, the transport properties predicted via the effective single particle DFT picture may also not be accurate. To our knowledge, no first-principles study have addressed how electron correlations affect the performances of prototypical spin-valves as, to date, there have been no computational platforms to address this question. The goal of this paper is to show how such platform can be built and then used to analyse the linear-response GMR in two-terminal devices beyond the DFT limitations.

A significant progress in the theoretical understanding of correlation effects in  $3d$  TMs has been achieved with the dynamical mean-field theory (DMFT)<sup>32-35</sup>. In the so-called LSDA+DMFT scheme<sup>35,36</sup>, LSDA calculations provide the *ab-initio* material dependent inputs (orbitals and hopping parameters), while DMFT solves the many-body problem for the local interactions. In the case of  $3d$  ferromagnetic TMs LSDA+DMFT has been applied to address spectral properties of bulk materials<sup>29,37</sup> and surfaces<sup>37</sup>, digital heterostructures<sup>38,39</sup>, alloys<sup>40</sup>, interfaces containing half-metallic ferromagnets<sup>41,42</sup> and to estimate magnetic moments above and below the

Curie temperature<sup>29</sup>. In all these studies LSDA+DMFT provides qualitative and quantitative improvements in the description of the systems electronic and magnetic properties compared to DFT. In the context of two-terminal devices, LSDA+DMFT has been applied to address linear-response transport properties in point contacts<sup>43–45</sup>, in molecular junctions<sup>46–50</sup>, and in heterostructures comprising a single correlated layer<sup>51,52</sup>, but, to our knowledge, never in TM-based spin-valves, which present several ferromagnetic layers.

In this paper, we describe the implementation of the LSDA+DMFT framework within the Smeagol quantum transport code<sup>27,53</sup> for studying transport through two-terminal nanoscale devices, and its application to magnetic multi-layered structures comprising 3*d* TMs. Our approach generalizes layer-DMFT, which so far has been used for models<sup>54–56</sup>, in order to deal with realistic systems, attached to electrodes, and from first-principles. In particular, we compute the spin-polarized conductance and the GMR in prototypical heterostructures with alternating Cu and Co layers, where we account for electron correlation effects in the Co 3*d* orbitals thus providing important indications about the role that these effects have on spin transport. LSDA+DMFT is integrated with the NEGF method, allowing for the calculation of the transmission function through a correlated device region. Second order perturbation theory in the electron-electron interaction  $U$  is employed as DMFT solver allowing for the fast evaluation of the self-energy directly on the real frequency axis with no needs of any analytic continuation schemes. Notably, LSDA+DMFT transport calculations carried out with our implementation and the perturbative solver are, in practice, only slightly more complicated and computationally demanding than standard DFT+NEGF calculations. The solver is accurate for moderately correlated materials such as those studied here, and where  $U$  is smaller than the band-width. Nonetheless, our code can be easily extended to include any other solver and then to treat also strongly correlated systems. We expect that this will pave the way towards systematic studies of correlation effects in transport.

The paper is organized as follows. To begin with we review the basic theory for quantum transport formulated in terms of the NEGF, its combination with DFT (Sec. II A), and the extensions to systems for which an effective single-particle picture is not appropriate (Sec. II B). We then present our numerical implementation of DMFT in Secs. II C, II D and II E, the basic equations for the perturbative impurity solver in Sec. II F), and the computational details in Sec. III. The results are presented in Sec. (IV). Specifically, we describe the DFT and LSDA+DMFT calculations for a single Co layer sandwiched between two Cu electrodes in Sec. IV A, and we study the GMR effect in a complex heterostructure in Sec. IV B. Finally we conclude.

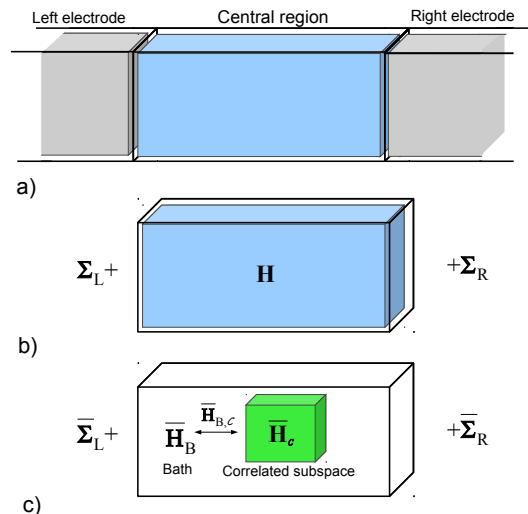


FIG. 1. (a) Schematic representation of a two-terminal device, which includes a central region (CR) placed between two semi-infinite electrodes. (b) The CR has Hamiltonian  $H^\sigma(\mathbf{k})$ , and the effect of the electrodes on the central region is described via the left and right electrode self-energies. Note that we do not indicate the spin index and the  $\mathbf{k}$ -dependence in the picture to maintain the notation lighter. (c) The correlated subspace of Hamiltonian  $\bar{H}_C^\sigma(\mathbf{k})$  can be separated from the rest of the CR, which we refer to as the bath. The correlated subspace and the bath are coupled through the coupling Hamiltonian  $\bar{H}_{B,c}^\sigma(\mathbf{k})$ .

## II. METHOD AND IMPLEMENTATION

### A. Transport via DFT+NEGF

The typical system that we consider is shown schematically in Fig. 1 and represents a two-terminal device. We set the transport direction along the  $z$  Cartesian axis. We employ a linear combination of atomic orbitals (LCAO) basis set. The system is divided in three parts: a central region (CR) and left ( $L$ ) and right ( $R$ ) electrodes, from which electrons flow in and out. To start with, we assume that electrons in both the CR and the electrodes are effectively non-interacting. Further, each electrode is semi-infinite and periodic away from the CR.  $\mathbf{k} = (k_x, k_y)$  indicates the wave-vector in the transverse direction.  $H^\sigma(\mathbf{k})$  then is the  $\mathbf{k}$ -dependent single-particle Hamiltonian of the CR for electrons of spin  $\sigma = \uparrow, \downarrow$  and  $S(\mathbf{k})$  is the orbital overlap, since in general the basis set is non-orthogonal. Note that we assume that there are no spin-mixing term in the Hamiltonian. We denote with  $N$  the number of basis orbitals of the CR.  $H^\sigma(\mathbf{k})$  and  $S(\mathbf{k})$  are therefore matrices of dimension  $N \times N$ . Each electrode is in local thermal equilibrium at its own chemical potential  $\mu_{L/R}$  due to its infinitely large size. When a bias voltage is applied, these chemical potentials are shifted as  $\mu_{L/R} = E_F \pm eV/2$ , where  $e$  is the electron charge and  $E_F$  is the Fermi energy when the system is in

thermodynamic equilibrium.

To describe the electronic structure and the quantum transport of the device, we use the non-equilibrium Green's function (NEGF) approach<sup>57</sup>. A crucial advantage of this method is that the CR can be separated out from the semi-infinite electrodes, whose effect is then captured via the momentum- and energy-dependent retarded electrode self-energies,  $\Sigma_L^\sigma(\mathbf{k}, E)$  and  $\Sigma_R^\sigma(\mathbf{k}, E)$ . Their antihermitian parts

$$\Gamma_{L/R}^\sigma(\mathbf{k}, E) = i[\Sigma_{L/R}^\sigma(\mathbf{k}, E) - \Sigma_{L/R}^{\sigma\dagger}(\mathbf{k}, E)] \quad (1)$$

represent the strength of the electronic coupling between the electrodes and the CR. The properties of the CR are then fully described by the retarded and lesser Green's functions, defined as

$$g^\sigma(\mathbf{k}, E) = [ES(\mathbf{k}) - H^\sigma(\mathbf{k}) - \Sigma_L^\sigma(\mathbf{k}, E) - \Sigma_R^\sigma(\mathbf{k}, E)]^{-1}, \quad (2)$$

$$g^{\sigma<}(\mathbf{k}, E) = g^\sigma(\mathbf{k}, E)[\Sigma_L^{\sigma<}(\mathbf{k}, E) + \Sigma_R^{\sigma<}(\mathbf{k}, E)]g^\sigma(\mathbf{k}, E)^\dagger, \quad (3)$$

where the lesser electrodes' self-energies are defined as

$$\Sigma_{L(R)}^{\sigma<}(\mathbf{k}, E) = if_{L(R)}(E)\Gamma_{L(R)}^\sigma(\mathbf{k}, E), \quad (4)$$

with  $f_{L/R}(E) = [e^{\beta(E-\mu_{L/R})} + 1]^{-1}$  the Fermi function of the left/right electrode; here  $\beta = 1/k_B\theta$ , with  $k_B$  representing the Boltzmann constant, and  $\theta$  the electronic temperature. The CR's Green's functions and self-energies are  $N \times N$  matrices like  $H^\sigma(\mathbf{k})$ .

The density matrix of the CR region is given by

$$\rho^\sigma = \frac{1}{N_{\mathbf{k}}} \sum_{\mathbf{k}} \left[ \frac{1}{2\pi i} \int dE g^{\sigma<}(\mathbf{k}, E) \right] \quad (5)$$

where  $N_{\mathbf{k}}$  is the number of  $\mathbf{k}$ -points in the Brillouin zone. In our calculations,  $H^\sigma(\mathbf{k})$  is the DFT Kohn-Sham Hamiltonian within the LSDA, and it is therefore density dependent. Eqs. (2), (3) and (5) need to be evaluated self-consistently<sup>26-28</sup>. This method is usually called DFT+NEGF, and it is the state-of-the-art approach to study spin-dependent transport through nanodevices. Here, we use the implementation of DFT+NEGF in the Smeagol transport code<sup>27,53</sup>, which obtains the LSDA Kohn-Sham Hamiltonian from the DFT package Siesta<sup>58</sup>. The current across the CR for electrons of spin  $\sigma$  is evaluated as<sup>26-28,57</sup>

$$I^\sigma = \frac{e}{h} \int T^\sigma(E) [f_L(E) - f_R(E)] dE, \quad (6)$$

where  $h$  is Planck's constant and

$$T^\sigma(E) = \frac{1}{N_{\mathbf{k}}} \sum_{\mathbf{k}} T^\sigma(\mathbf{k}, E), \quad (7)$$

$$T^\sigma(\mathbf{k}, E) = \text{Tr} \left[ \Gamma_L^\sigma(\mathbf{k}, E) g^\sigma(\mathbf{k}, E)^\dagger \Gamma_R^\sigma(\mathbf{k}, E) g^\sigma(\mathbf{k}, E) \right]$$

is the spin- and energy-dependent transmission function. The conductance,  $\mathfrak{G}$ , at zero temperature ( $\theta = 0$ ) and in the linear-response limit  $\mu_L - \mu_R \rightarrow 0$ , also denoted

as zero-bias limit, reduces to the well-known Landauer formula

$$\mathfrak{G} = \frac{\mathfrak{G}_0}{2} \sum_{\sigma} T^\sigma(E_F), \quad (8)$$

where  $\mathfrak{G}_0 = 2e^2/h$  is the quantum of conductance. Notably, for non-interacting electrons, it has been proved that the Landauer and the so-called Kubo approaches are equivalent<sup>59</sup>, so that the linear-response transport properties of a system can be computed with either formalism.

## B. Transport through a correlated central region

When the CR is not appropriately described by the effective single-particle picture, the DFT+NEGF method presented above needs to be extended by adding to Eqs. (2) and (3) the many-body retarded and lesser self-energies,  $\Sigma_{MB}^\sigma(\mathbf{k}, E)$  and  $\Sigma_{MB}^{\sigma<}(\mathbf{k}, E)$ <sup>60</sup>. Thus the retarded and lesser Green's functions for the interacting system become<sup>61-63</sup>

$$G^\sigma(\mathbf{k}, E) = [ES(\mathbf{k}) - H^\sigma(\mathbf{k}) - \Sigma_L^\sigma(\mathbf{k}, E) - \Sigma_R^\sigma(\mathbf{k}, E) - \Sigma_{MB}^\sigma(\mathbf{k}, E)]^{-1}, \quad (9)$$

and

$$G^{\sigma<}(\mathbf{k}, E) = G^\sigma(\mathbf{k}, E) [\Sigma_L^{\sigma<}(\mathbf{k}, E) + \Sigma_R^{\sigma<}(\mathbf{k}, E) + \Sigma_{MB}^{\sigma<}(\mathbf{k}, E)] G^\sigma(\mathbf{k}, E)^\dagger. \quad (10)$$

Eq. (9) can be re-expressed as a Dyson equation

$$G^\sigma(\mathbf{k}, E) = g^\sigma(\mathbf{k}, E) + g^\sigma(\mathbf{k}, E) \Sigma_{MB}(\mathbf{k}, E) G^\sigma(\mathbf{k}, E), \quad (11)$$

which allows to obtain the retarded many-body Green's function, also called dressed Green's function, from the non-interacting, or bare, Green's function  $g^\sigma(\mathbf{k}, E)$  of Eq. (2).

The formal introduction of the many-body self-energies shows that the electron-electron interaction effectively acts on the system as an additional electrode. We can then define the effective "coupling" matrix<sup>47</sup>

$$\Gamma_{MB}^\sigma(\mathbf{k}, E) = i[\Sigma_{MB}^\sigma(\mathbf{k}, E) - \Sigma_{MB}^{\sigma\dagger}(\mathbf{k}, E)], \quad (12)$$

and express  $\Sigma_{MB}^{\sigma<}(\mathbf{k}, E)$  as<sup>47</sup>

$$\Sigma_{MB}^{\sigma<}(\mathbf{k}, E) = iF_{MB}^\sigma(\mathbf{k}, E)\Gamma_{MB}^\sigma(\mathbf{k}, E). \quad (13)$$

This equation has the same structure as Eq. (4), but  $F_{MB}^\sigma(\mathbf{k}, E)$  is a matrix, which describes the out-of-equilibrium distribution of the interacting electrons in the CR, and it is not the Fermi function. The resulting current was first computed by Meir and Wingreen in a seminal work<sup>64</sup>, and can be written as<sup>47</sup>

$$I^\sigma = I_c^\sigma + I_{nc}^\sigma. \quad (14)$$

$I_c^\sigma$  is the coherent contribution expressed as in Eq. (6), but with the transmission function evaluated with the retarded dressed Green's function, i.e.

$$T_{MB}^\sigma(\mathbf{k}, E) = \text{Tr} \left[ \Gamma_L^\sigma(\mathbf{k}, E) G^\sigma(\mathbf{k}, E)^\dagger \Gamma_R^\sigma(\mathbf{k}, E) G^\sigma(\mathbf{k}, E) \right]. \quad (15)$$

$I_{nc}^\sigma$  is the non-coherent contribution and reads<sup>47,65</sup>

$$I_{nc}^\sigma = \text{Tr} \left\{ [F_{MB}^\sigma(\mathbf{k}, E) - f_R(E)] \times \Gamma_{MB}^\sigma(\mathbf{k}, E) G^\sigma(\mathbf{k}, E)^\dagger \Gamma_{MB}^\sigma(\mathbf{k}, E) G^\sigma(\mathbf{k}, E) \right\}. \quad (16)$$

It accounts for the effect of the ‘‘interaction electrode’’. Electrons can be effectively seen as entering the interaction electrode, where they undergo some scattering processes losing coherence, before being finally re-injected into the system<sup>66</sup>. The mathematical form of  $I_{nc}^\sigma$  resembles that of  $I_c^\sigma$ . However,  $F_{MB}^\sigma(\mathbf{k}, E)$  can not be brought outside the trace, and we cannot define a transmission function related to the flow of electrons from the interaction electrode into the right electrode<sup>65</sup>.

In this paper, we focus on the linear-response limit, and neglect non-coherent contributions to the conductance. The calculation of such non-coherent contributions is an open problem. To date, it has only been solved assuming a specific shape for the matrix  $F_{MB}^\sigma(\mathbf{k}, E)$ <sup>61,67</sup>, or that the CR has a single atom and orbital, so that  $\Gamma_{L/R}^\sigma$  are numbers instead of matrices<sup>64</sup>. In the linear-response Kubo formalism, neglecting non-coherent contributions would mean neglecting vertex corrections<sup>68</sup>, which in general increase the conductivity. We are not aware of any first-principles study where these vertex corrections to the conductivity have been evaluated and included.

The transmission function  $T_{MB}^\sigma(\mathbf{k}, E_F)$  is calculated with the retarded dressed Green's function evaluated in thermodynamics equilibrium. The fluctuation-dissipation theorem holds and gives<sup>60</sup>

$$G^{\sigma<}(\mathbf{k}, E) = if(E)D^\sigma(\mathbf{k}, E), \quad (17)$$

where  $f(E) = f_L(E) = f_R(E)$ , and

$$D^\sigma(\mathbf{k}, E) = i[G^\sigma(\mathbf{k}, E) - G^\sigma(\mathbf{k}, E)^\dagger] \quad (18)$$

is the spectral function. Thus, only  $G^\sigma(\mathbf{k}, E)$  is required to fully describe the system. In summary, solving the interacting problem and calculating the linear response transport within the mentioned approximations reduces to the evaluation of the retarded self-energy  $\Sigma_{MB}(\mathbf{k}, E)$  and of the Dyson Eq. (11).

### C. Projection to the correlated subspace

The discussion in the previous subsection provided the formal equations to study transport in correlated nano-devices. However, calculations including all the orbitals of the CR represent in practice a great challenge. To simplify the problem, we note that only states near the Fermi

level play an important role in transport at low bias voltages [see Eq. (8)]. Hence, all those other states, that are either much higher or lower in energy, can be integrated out. In case of metallic TM-based spin-valves, there are 4s and 3d states at the Fermi level. 4s states are delocalized, the bands have a large dispersion and electronic correlations are well described at the effective single-particle Kohn-Sham level. In contrast, open 3d shells of the ferromagnetic TM layers are more tightly bound to the ionic cores and, as such, they are moderately correlated. We then define the ‘‘correlated subspace’’ ( $\mathcal{C}$ ) as the subspace of the CR that includes all 3d orbitals. Assuming that there are  $N_{\text{TM}}$  TM atoms inside the CR, the correlated subspace  $\mathcal{C}$  will have dimension  $2(5 \times N_{\text{TM}})$  (the factor 2 accounts for the spin). The CS can be projected out from the rest of the system, which we refer to as the ‘‘bath’’ ( $\mathcal{B}$ ), and which includes the orthogonal subspace to  $\mathcal{C}$  within both the CR and electrodes. To carry out such projection, we use the scheme presented in Ref. 47, and we perform the basis change, which transforms the SR overlap and Hamiltonian matrix as

$$\begin{aligned} \bar{S}(\mathbf{k}) &= \begin{pmatrix} 1 & 0 \\ 0 & \bar{S}_{\mathcal{B}}(\mathbf{k}) \end{pmatrix} = \\ &= W(\mathbf{k})^\dagger S(\mathbf{k}) W(\mathbf{k}), \end{aligned} \quad (19)$$

$$\begin{aligned} \bar{H}^\sigma(\mathbf{k}) &= \begin{pmatrix} \bar{H}_{\mathcal{C}}^\sigma(\mathbf{k}) & \bar{H}_{\mathcal{C},\mathcal{B}}^\sigma(\mathbf{k}) \\ \bar{H}_{\mathcal{B},\mathcal{C}}^\sigma(\mathbf{k}) & \bar{H}_{\mathcal{B}}^\sigma(\mathbf{k}) \end{pmatrix} = \\ &= W(\mathbf{k})^\dagger H^\sigma(\mathbf{k}) W(\mathbf{k}). \end{aligned} \quad (20)$$

In the transformed matrices  $\bar{S}(\mathbf{k})$  and  $\bar{H}^\sigma(\mathbf{k})$  the top left block describes the correlated subspace  $\mathcal{C}$ , the bottom right block describes the part of the bath included in the CR, and the off-diagonal blocks describe the connection terms. The matrices  $W(\mathbf{k})$  are defined in Eq. (10) of Ref. 47. The transformation is designed in such a way that the orbitals of  $\mathcal{C}$  become orthogonal, and that they have zero overlap with the bath orbitals [see Eq. (19)].  $\bar{H}_{\mathcal{C}}^\sigma(\mathbf{k})$  in Eq. (20) is the non-interacting Hamiltonian matrix of  $\mathcal{C}$  with dimension  $5N_{\text{TM}} \times 5N_{\text{TM}}$ . Using the second quantization formalism, we can also write the Hamiltonian operator of  $\mathcal{C}$

$$\hat{H}_{\mathcal{C}}^\sigma(\mathbf{k}) = \sum_{i,j,\lambda_1,\lambda_2,\sigma} [\bar{H}_{\mathcal{C}}^\sigma(\mathbf{k})]_{i\lambda_1,j\lambda_2} \hat{d}_{i\lambda_1\sigma}^\dagger \hat{d}_{j\lambda_2\sigma}, \quad (21)$$

where  $\hat{d}_{i\lambda\sigma}^\dagger$  and  $\hat{d}_{i\lambda\sigma}$  are the electron creation and annihilation operators at orbital  $\lambda$  within the atom  $i$  and spin  $\sigma$  ( $i = 1, \dots, N_{\text{TM}}$  and  $\lambda = 1, \dots, 5$ ,  $\sigma = \uparrow, \downarrow$ ).  $[\bar{H}^\sigma(\mathbf{k})]_{i\lambda_1,j\lambda_2}$  is the Hamiltonian matrix element between the  $d$  orbital  $\lambda_1$  of the atom  $i$  and the  $d$  orbital  $\lambda_2$  of the atom  $j$ . Then, to describe the electron-electron interaction for the electrons in  $\mathcal{C}$ , we add an explicit Coulomb term as follow

$$\begin{aligned} \hat{H}_{\mathcal{C},U}^\sigma(\mathbf{k}) &= \hat{H}_{\mathcal{C}}^\sigma(\mathbf{k}) - \hat{H}_{\mathcal{C},dc}^\sigma + \\ &+ \frac{1}{2} \sum_{\substack{i,\lambda_1,\lambda_2,\lambda_3, \\ \lambda_4,\sigma_1,\sigma_2}} U_{\lambda_1,\lambda_2,\lambda_3,\lambda_4} \hat{d}_{i\lambda_1\sigma_1}^\dagger \hat{d}_{i\lambda_2\sigma_2}^\dagger \hat{d}_{i\lambda_4\sigma_2} \hat{d}_{i\lambda_3\sigma_1}, \end{aligned} \quad (22)$$

where  $U_{\lambda_1, \lambda_2, \lambda_3, \lambda_4}$  are the four-index Hubbard- $U$  matrix elements, which account for the screened Coulomb interaction between four  $3d$  orbitals located on the same atom.  $U_{\lambda_1, \lambda_2, \lambda_3, \lambda_4}$  are parametrized in terms of the average effective Coulomb interaction  $U$  and exchange  $J$ <sup>69</sup>

$$U = \frac{1}{(2l+1)^2} \sum_{\lambda_1, \lambda_2} U_{\lambda_1, \lambda_2, \lambda_1, \lambda_2} \quad (23)$$

$$J = \frac{1}{2l(2l+1)} \sum_{\lambda_1 \neq \lambda_2, \lambda_2} U_{\lambda_1, \lambda_2, \lambda_2, \lambda_1}. \quad (24)$$

The reason for using the multi-orbital Hubbard-like form is the local nature of the screened Coulomb interaction, which allows us to ignore the Coulomb integrals involving correlated orbitals of different atoms.  $\bar{H}_{\mathcal{C}, dc}^\sigma$  is the double-counting correction, which is needed to cancel the Coulomb interactions already taken into account in the LSDA exchange-correlation potential. The exact form of the double-counting correction is not known, but several approximations have been proposed and are used in practice<sup>29,35,70,71</sup>. From a pragmatic point of view we consider to include the double counting correction into the on-site energy shift as described in Sec. II G.

#### D. Green's function and many-body self-energy of the correlated subspace

The bare and dressed Green's function,  $g^\sigma(\mathbf{k}, E)$  and  $G^\sigma(\mathbf{k}, E)$ , are expressed in the transformed basis set formally introduced in the previous section as<sup>47</sup>

$$\begin{aligned} \bar{g}^\sigma(\mathbf{k}, E) &= \begin{pmatrix} \bar{g}_{\mathcal{C}}^\sigma(\mathbf{k}, E) & \bar{g}_{\mathcal{C}, \text{B}}^\sigma(\mathbf{k}, E) \\ \bar{g}_{\text{B}, \mathcal{C}}^\sigma(\mathbf{k}, E) & \bar{g}_{\text{B}}^\sigma(\mathbf{k}, E) \end{pmatrix} = \\ &= W(\mathbf{k})^{-1} g^\sigma(\mathbf{k}, E) W(\mathbf{k})^{-1\dagger} \end{aligned} \quad (25)$$

and

$$\begin{aligned} \bar{G}^\sigma(\mathbf{k}, E) &= \begin{pmatrix} \bar{G}_{\mathcal{C}}^\sigma(\mathbf{k}, E) & \bar{G}_{\mathcal{C}, \text{B}}^\sigma(\mathbf{k}, E) \\ \bar{G}_{\text{B}, \mathcal{C}}^\sigma(\mathbf{k}, E) & \bar{G}_{\text{B}}^\sigma(\mathbf{k}, E) \end{pmatrix} = \\ &= W(\mathbf{k})^{-1} G^\sigma(\mathbf{k}, E) W(\mathbf{k})^{-1\dagger}, \end{aligned} \quad (26)$$

where  $W(\mathbf{k})^{-1}$  is the inverse of the transformation matrix used in Eqs. (19) and (20).  $\bar{g}^\sigma(\mathbf{k}, E)$  and  $\bar{G}^\sigma(\mathbf{k}, E)$  have the same block structure as the Hamiltonian matrix in Eq. (20). The blocks  $\bar{g}_{\mathcal{C}}^\sigma(\mathbf{k}, E)$  and  $\bar{G}_{\mathcal{C}}^\sigma(\mathbf{k}, E)$  are the Green's function matrices of the correlated subspace. They satisfy the Dyson equation for the correlated subspace

$$\bar{G}_{\mathcal{C}}^\sigma(\mathbf{k}, E) = [\bar{g}_{\mathcal{C}}^\sigma(\mathbf{k}, E)^{-1} - \bar{\Sigma}_{\mathcal{C}}^\sigma(\mathbf{k}, E)]^{-1}, \quad (27)$$

where  $\bar{\Sigma}_{\mathcal{C}}^\sigma(\mathbf{k}, E)$  is the many-body self-energy of  $\mathcal{C}$ . This formally specifies the many-body correlation inside  $\mathcal{C}$  due to the interaction in Eq. (22). In the following sections we will see how  $\bar{\Sigma}_{\mathcal{C}}^\sigma(\mathbf{k}, E)$  is computed in practice. From  $\bar{\Sigma}_{\mathcal{C}}^\sigma(\mathbf{k}, E)$  we can easily obtain the many-body self-energy of whole CR. In the transformed basis, this is

$$\bar{\Sigma}_{MB}^\sigma(\mathbf{k}, E) = \begin{pmatrix} \bar{\Sigma}_{\mathcal{C}}^\sigma(\mathbf{k}, E) & 0 \\ 0 & 0 \end{pmatrix}, \quad (28)$$

since the bath is non-interacting by assumption. In the original basis the CR many-body self-energy is obtained by performing

$$\Sigma_{MB}^\sigma(\mathbf{k}, E) = W(\mathbf{k})^{-1\dagger} \bar{\Sigma}_{MB}^\sigma(\mathbf{k}, E) W(\mathbf{k})^{-1}. \quad (29)$$

#### E. DMFT

The many-body problem within the correlated subspace  $\mathcal{C}$  is solved via DMFT, which means that we only consider electron correlation local in space. The self-energy  $\bar{\Sigma}_{\mathcal{C}}^\sigma(\mathbf{k}, E)$  of  $\mathcal{C}$  is therefore approximated by the DMFT self-energy

$$\bar{\Sigma}_{\mathcal{C}, DMFT}^\sigma(E) = \begin{pmatrix} \bar{\Sigma}_1^\sigma(E) & 0 & \dots & 0 \\ 0 & \bar{\Sigma}_2^\sigma(E) & \dots & 0 \\ 0 & 0 & \dots & \bar{\Sigma}_{N_{\text{TM}}}^\sigma(E) \end{pmatrix}, \quad (30)$$

where  $\bar{\Sigma}_i^\sigma(E)$  is the  $5 \times 5$  block for the  $3d$  orbitals of the atom  $i$ . We note that, in general, each block  $\bar{\Sigma}_i^\sigma(E)$  can be non-diagonal. Eq. (30) generalizes to multi-orbital systems the DMFT self-energy used in layer-DMFT for tight-binding models<sup>54,55,72</sup>. Practically  $\bar{\Sigma}_{\mathcal{C}, DMFT}^\sigma(E)$  is computed by mapping the correlated subspace into a set of auxiliary impurity problems, one per atom. Each impurity is numerically solved obtaining the correspondent (local) many-body self-energies  $\bar{\Sigma}_i^\sigma(E)$ . The procedure is embedded into a self-consistency loop shown in Fig. 2. In our implementation, the CR space is down-folded into the correlated subspace at each DMFT iteration and, after solving the impurity problem, the self-energy is transformed back to the original space. This is an approach that follows previous implementations of LSDA+DMFT for periodic systems<sup>73-77</sup>. The self-consistent DMFT loop is summarized as follows:

- i) We compute the dressed CR Green's function  $G^\sigma(\mathbf{k}, E)$  in Eq. (9). In the first iteration, we use a guess for the many-body self-energy; here we use  $\Sigma_{MB}^\sigma(\mathbf{k}, E) = 0$  for this initial step.
- ii) We carry out the transformation in Eq. (26), and we separate the Green's function of the correlated subspace  $\bar{G}_{\mathcal{C}}^\sigma(\mathbf{k}, E)$ .
- iii) We define the so-called local Green's function

$$\bar{G}_{\text{loc}}^\sigma(E) = \frac{1}{N_{\mathbf{k}}} \sum_{\mathbf{k}} \bar{G}_{\mathcal{C}}^\sigma(\mathbf{k}, E). \quad (31)$$

- iv) We build the  $5 \times 5$  dynamical field matrix  $\mathcal{G}_i^\sigma(E)$  for each atom  $i$  in the CS:

$$\mathcal{G}_i^\sigma(E) = \{[\bar{G}_{\text{loc}, i}^\sigma(E)]^{-1} + \bar{\Sigma}_i^\sigma(E)\}^{-1}, \quad (32)$$

where  $\bar{G}_{\text{loc}, i}^\sigma(E)$  is the  $5 \times 5$  block of the local Green's function matrix relative to the atom  $i$ .

- v) We map each of the  $N_{\text{TM}}$  atom inside the  $\mathcal{C}$  into an Anderson impurity model. This is done by defining the bare impurity Green's function of atom  $i$  as  $g_{\text{imp},i}^{\sigma}(E) = \mathcal{G}_i^{\sigma}(E)$ .
- vi) We solve the impurity problems as described in Sec. IIF, and with that we obtain the impurity many-body self-energies  $\Sigma_{\text{imp},i}^{\sigma}(E)$ .
- vii) We set  $\bar{\Sigma}_i^{\sigma}(E) = \Sigma_{\text{imp},i}^{\sigma}(E)$  for each atom  $i$ , and we then compute the DMFT self-energy in Eq. (30).
- viii) We “unfold” the self-energy to the original basis using Eq. (29). This gives the updated CR many-body self-energy  $\Sigma_{MB}(\mathbf{k}, E)$ . We then go back to step i) to start the next iteration.

After converging the self-consistent DMFT equations, we compute the CR density of states as

$$\text{DOS}^{\sigma}(E) = \frac{1}{N_{\mathbf{k}}} \sum_{\mathbf{k}} D(\mathbf{k}, E), \quad (33)$$

and the transmission function defined in Eq. (15). We note that in our implementation the self-energy is made off-diagonal and momentum-dependent at each DMFT iteration, because of the transformation in Eq. (29).

### F. Solution of the impurity problem

As outlined in the previous section, DMFT requires the solution of auxiliary impurity problems to determine the self-energies  $\bar{\Sigma}_i^{\sigma}(E) = \Sigma_{\text{imp},i\lambda}^{\sigma}(E)$ . The impurity solvers generally used for ferromagnetic metals, such as continuous time quantum Monte Carlo<sup>78</sup> or the spin-polarized  $T$ -matrix fluctuating exchange approximation<sup>79–82</sup>, are formulated on the imaginary frequency axis. Spectral functions are obtained indirectly via the numerical analytical continuation to the real energy axis<sup>83–86</sup>. Unfortunately, this often leads to numerical difficulties, since the

analytical continuation of discrete numerical data is not unambiguous. Moreover, it necessitates the appropriate treatment of the high-frequency “tails”<sup>87</sup>. These issues become even more pressing in case of transport calculations, since the evaluation of the transmission function in Eq. (15), and therefore of the conductance, requires accurate retarded Green's functions for real energies. For this reason, here we consider the second order perturbative treatment proposed in Refs. 88 and 89, and which can be implemented to provide the self-energy directly on the real energy axis, while retaining the multi-orbital nature of the many-body problem. In spite of its computational efficiency, in Ref. 89 we showed that the second order self-energy contributions already accounts for all characteristic spectroscopic features caused by electron correlation in ferromagnetic transition metals.

The systems considered in this paper have diagonal dynamical field matrices  $\mathcal{G}_i^{\sigma}(E) = g_{\text{imp},i}^{\sigma}(E)$  in Eq. (32) because of symmetry. This greatly reduces the computational effort. We denote the diagonal elements of many-body self-energy,  $[\Sigma_i^{\sigma}(E)]_{\lambda,\lambda}$ , for the orbital  $\lambda$  of atom  $i$  as  $\Sigma_{i\lambda}^{\sigma}(E) \equiv [\Sigma_i^{\sigma}(E)]_{\lambda,\lambda}$ . Then, the self-energy up to the second order in diagrammatic perturbation theory in  $U$  over the band width is written as

$$\Sigma_{i\lambda}^{\sigma}(E) \approx \Sigma_{i\lambda}^{\sigma(1)} + \Sigma_{i\lambda}^{\sigma(2)}(E). \quad (34)$$

The first-order contribution is

$$\Sigma_{i\lambda}^{\sigma(1)} = \sum_{\lambda_1 \sigma_1} U_{\lambda\lambda_1\lambda\lambda_1} n_{i\lambda_1}^{\sigma_1} - \sum_{\lambda_1} U_{\lambda\lambda_1\lambda_1\lambda} n_{i\lambda_1}^{\sigma}, \quad (35)$$

and is the well-known Hartree-Fock approximation, where  $n_{i\lambda}^{\sigma} = \int_{-\infty}^{\infty} dE f(E) \text{Im} g_{\text{imp},i\lambda}^{\sigma}(E)$  is the occupation of the orbital  $\lambda$  of spin  $\sigma$  for the impurity  $i$ ;  $f(E)$  is the Fermi function.  $\Sigma_{i\lambda}^{\sigma(1)}$  is local in time, i.e. frequency independent. It therefore represents a one-electron potential producing only a shift of the non-interacting energy levels.

The second order self-energy  $\Sigma_{i\lambda}^{\sigma(2)}(E)$  can be split into its real and imaginary parts. The imaginary part is given by<sup>90</sup>

$$\begin{aligned} \text{Im} \left[ \Sigma_{i\lambda}^{\sigma(2)}(E) \right] = & -\pi \sum_{\lambda_1 \lambda_2 \lambda_3 \sigma_1} U_{\lambda\lambda_1\lambda_2\lambda_3} U_{\lambda_3\lambda_2\lambda_1\lambda} \int_{-\infty}^{\infty} d\epsilon_1 \int_{-\infty}^{\infty} d\epsilon_2 D_{i\lambda_1}^{\sigma_1}(\epsilon_1) D_{i\lambda_2}^{\sigma}(\epsilon_2) D_{i\lambda_3}^{\sigma_1}(\epsilon_1 + \epsilon_2 - E) \times \\ & \{ f(\epsilon_1) f(\epsilon_2) + [1 - f(\epsilon_1) - f(\epsilon_2)] f(\epsilon_1 + \epsilon_2 - E) \} \\ & + \pi \sum_{\lambda_1 \lambda_2 \lambda_3} U_{\lambda\lambda_1\lambda_2\lambda_3} U_{\lambda_2\lambda_3\lambda_1\lambda} \int_{-\infty}^{\infty} d\epsilon_1 \int_{-\infty}^{\infty} d\epsilon_2 D_{i\lambda_1}^{\sigma}(\epsilon_1 + \epsilon_2 - E) D_{i\lambda_2}^{\sigma}(\epsilon_2) D_{i\lambda_3}^{\sigma}(\epsilon_1) \times \\ & \{ f(\epsilon_2) f(\epsilon_1) + [1 - f(\epsilon_2) - f(\epsilon_1)] f(\epsilon_1 + \epsilon_2 - E) \}, \end{aligned} \quad (36)$$

where

$$D_{i\lambda}^{\sigma}(E) = -\frac{1}{\pi} \text{Im} [g_{\text{imp},i\lambda}^{\sigma}(E)] \quad (37)$$

is the spectral function of  $g_{\text{imp},i\lambda}(E)$ . The real part is computed by the Kramers-Kronig relations as

$$\text{Re} \left[ \Sigma_{i\lambda}^{\sigma(2)}(E) \right] = -\frac{1}{\pi} \int_{-\infty}^{\infty} d\epsilon \frac{\text{Im} \left[ \Sigma_{i\lambda}^{\sigma(2)}(\epsilon) \right]}{E - \epsilon}. \quad (38)$$

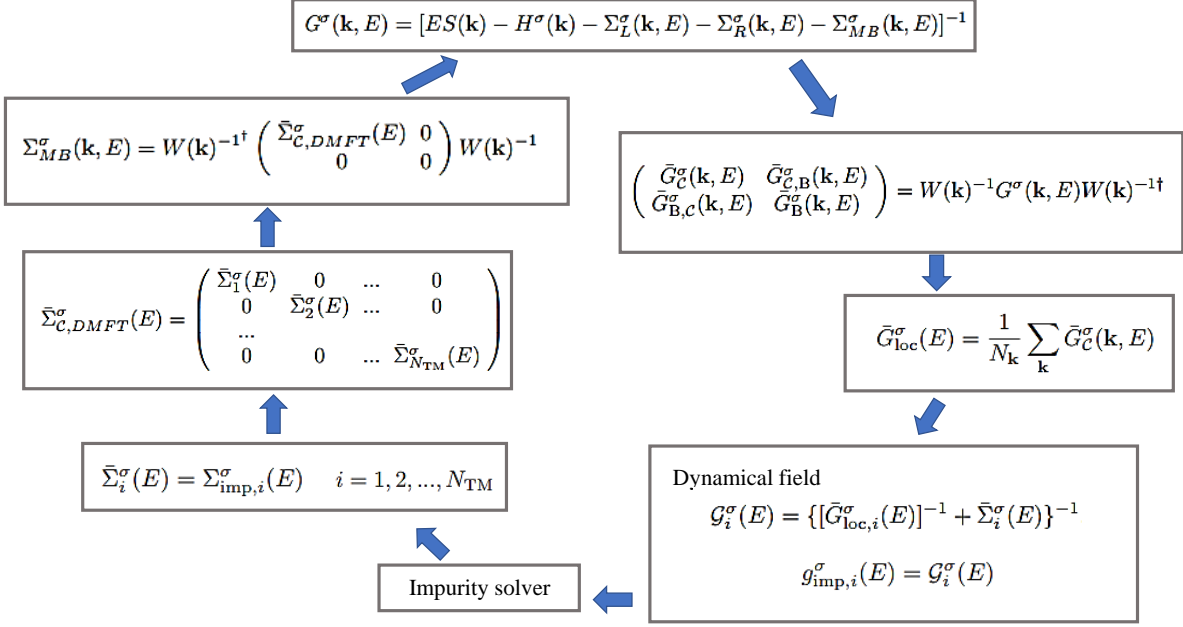


FIG. 2. Schematic representation of the DMFT self-consistent loop.

Details about the implementation and numerical calculations are presented in Ref. 89. We note that the dressed impurity Green's function

$$G_{i\lambda}^{\sigma}(E)^{-1} = g_{i\lambda}^{\sigma}(E)^{-1} - \Sigma_{i\lambda}^{\sigma}(E) \quad (39)$$

instead of the bare  $g_{i\lambda}^{\sigma}(E)$  could be used in the evaluation of self-energy contributions<sup>60</sup>. This would require a self-consistent solution of Eqs. (39), (35), and (36). In this paper, we do not carry out that to reduce the computational cost of the calculations. In practice we neglect some of the second order diagrams in the perturbative expansion<sup>60</sup> and, therefore, some multi-band screening effects. However, these effects are expected to be quite small<sup>89</sup> and not particularly important for the goals of this paper.

Finally we would like to remark that, although we consider here only moderately correlated systems, for which perturbation theory in  $U$  is valid, our DMFT algorithm in Sec. II E is applicable to general systems, including nano-junctions comprising strongly correlated materials. In that case, different approximations for the impurity solver beyond the second-order approximation will be required. For example one may employ the non-crossing<sup>91,92</sup> and the one-crossing approximations<sup>93,94</sup>, which can be implemented to provide the self-energy directly on the real frequency axis, while retaining the multi-orbital nature of the many-body problem<sup>45,71</sup>.

### G. On-site energy shift and the problem of the double-counting

DFT+NEGF calculations are performed in the grand-canonical ensemble. Here, rather than fixing the total number of electrons inside the CR, the Fermi energy is fixed by the chemical potential of the electrodes,  $E_F = \mu_L = \mu_R$ . The total number of electrons in the CR typically fluctuates during the charge self-consistent DFT cycle until it eventually converges to the nominal value given by the sum of the various CR atomic valence (+core) electrons for pseudopotentials-based (all-electron) implementations. A similar behaviour is expected also in charge self-consistent LSDA+DMFT two-terminal device calculations. However, such charge self-consistent LSDA+DMFT calculations are computationally too demanding for realistic systems like those studied here. In line with typical calculations for periodic systems, we therefore perform self-energy self-consistent DMFT calculations, but we do not iterate the evaluation of the charge density. The total number of electrons of the CR is found to deviate slightly from the nominal value. To reimpose the correct electron counting for periodic systems, one usually adjusts the chemical potential of the impurity until the correct occupation is obtained. We adapt this process to the transport setup by adding an identical on-site potential  $v$  to all correlated  $3d$  orbitals. In other words, we readjust the real part of the many self-energy as  $\text{Re}[\Sigma_{i\lambda}^{\sigma}(E)] \rightarrow \text{Re}[\Sigma_{i\lambda}^{\sigma}(E)] + v$ . The potential  $v$  incorporates an effective double-counting correction for two-terminal device set-ups. We stress that this is an ad-hoc adjustment based on the electron

counting. Yet, preliminaries studies, albeit for different and simpler systems, seem to suggest that such adjustment reproduces quite well the results of fully charge self-consistent calculations<sup>95</sup>. To our best knowledge the formulation of a specific double-counting scheme for a two-terminal device has not yet been implemented and this does not constitute the goal of the present study.

### III. COMPUTATIONAL DETAILS

DFT calculations are performed treating core electrons with norm-conserving Troullier-Martin pseudopotentials. The valence states are expanded through a numerical atomic orbital basis set including multiple- $\zeta$  and polarized functions<sup>58</sup>. The electronic temperature is set to 300 K. The real space mesh is set by an equivalent energy cutoff of 300 Ry. We use a  $12 \times 12$   $\mathbf{k}$ -point mesh to compute the self-consistent charge density with DFT. This charge density is then used as input in a non-self-consistent DFT calculation to obtain the density of states employing  $80 \times 80$   $\mathbf{k}$ -points. We shift all energies in such a way to set the Fermi level at 0 eV. DMFT calculations are performed using the bare Green's function  $g(\mathbf{k}, E)$  of Eq. (25) calculated for  $32 \times 32$   $\mathbf{k}$ -points. The temperature is 300 K. To calculate the second-order self-energy, we use an energy grid comprising 3200 points, and extending from  $-12$  to 6 eV. We express the Coulomb parameters  $U_{\lambda_1, \lambda_2, \lambda_3, \lambda_4}$  in terms of Slater integrals  $F^0$ ,  $F^2$  and  $F^4$  (Ref. 96). These are connected to the average effective Coulomb and exchange interactions of Eqs. (23) and (24) through the relations  $U = F^0$  and  $J = (F^2 + F^4)/14$ . The ratio  $F^4/F^2$  is assumed to correspond to the atomic value  $\approx 0.625$  (Ref. 97).

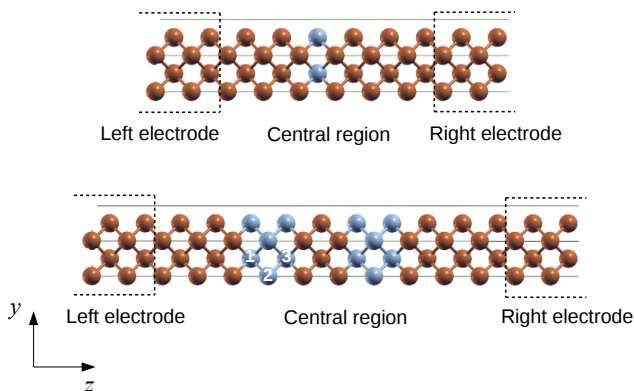


FIG. 3. Cu/Co/Cu (top panel) and Cu/Co<sub>3</sub>/Cu<sub>3</sub>/Co<sub>3</sub>/Cu (bottom panel) two terminal devices. The atoms Co 1, 2 and 3 in Cu/Co<sub>3</sub>/Cu<sub>3</sub>/Co<sub>3</sub>/Cu are labelled in the figure.

## IV. RESULTS

We now apply LSDA DFT and LSDA+DMFT to heterostructures presenting alternating Cu and Co layers, sandwiched between semi-infinite Cu electrodes. The goal is to illustrate the capabilities of our implementation of LSDA+DMFT and, in doing so, to gain some general understanding about the impact of electron correlation effects on linear-response spin transport properties. We first consider a single Co layer, and then investigate a more complex heterostructure, whose central region comprises two Co trilayers separated by a Cu spacer, and we compute its magnetoresistance.

The correlated subspace includes only the Co  $3d$  orbitals, while the Cu  $3d$  orbitals are considered uncorrelated, since they are fully filled and located in energy at about 2 eV below the Fermi level. The average Coulomb and exchange interactions are set to  $U = 1.5$  eV and  $J = 0.5$  eV, which give a splitting of the majority and minority DOS similar to that obtained in calculations<sup>51</sup> based on the exact muffin-tin orbitals (EMTO)-DMFT method<sup>98–101</sup>, with parameters that are established in that framework. The effective interaction is much smaller than the  $d$  band width, and the perturbative expansion used in the impurity solver is valid.

### A. Correlated Co monolayer

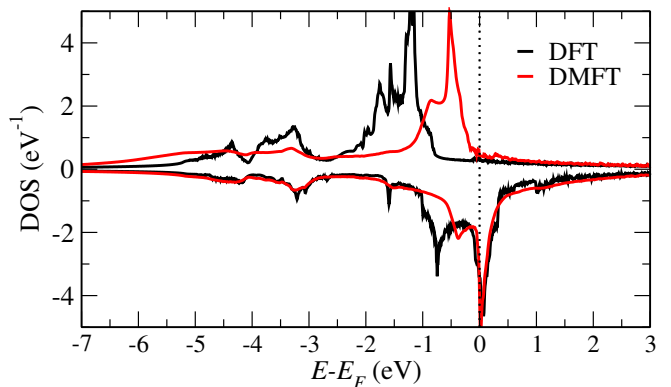


FIG. 4. DOS of the Co layer in the Cu/Co/Cu system, calculated by using DFT and DMFT (with  $U = 1.5$  eV and  $J = 0.5$  eV).

We denote the system as Cu/Co/Cu. Its simulation cell is shown in Fig. 3. The transport direction  $z$  is oriented along the Cu(100) orientation. The density of states (DOS) of the Co monolayer is shown in Fig. 4. We first consider the results of the LSDA DFT calculations. In the majority (spin up) channel, the  $d$ -states are fully occupied, and the DOS presents two main features. The first is a rather sharp peak, located in energy at  $E - E_F \approx -1.2$  eV, and followed by a “shoulder” at



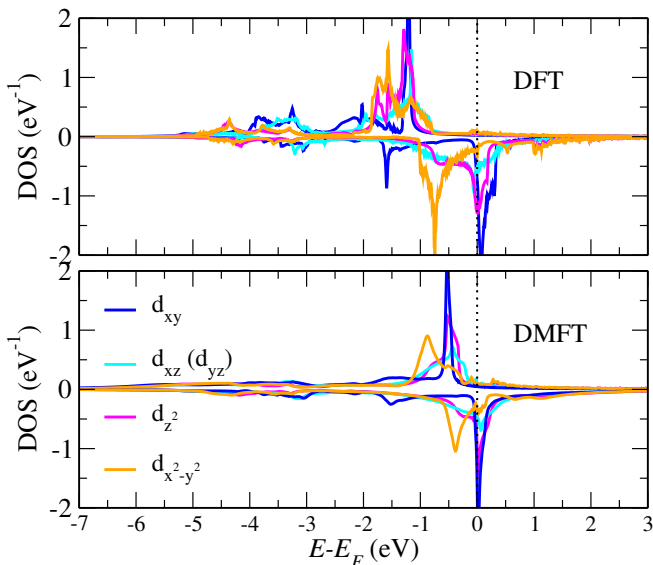


FIG. 5. DOS projected over the five Co  $d$  orbitals for the Cu/Co/Cu system. Top panel: DFT calculation; bottom panel: DMFT calculation.

about  $E - E_F \approx -1.7$  eV. The second feature is centered at  $E - E_F \approx -3.5$  eV, is broader and is followed by an additional lower peak at  $E - E_F \approx -4.3$  eV. Their character is understood by analyzing the orbital-resolved DOS in Fig. 5. The Co  $d_{xy}$ ,  $d_{xz}$  and  $d_{yz}$  orbitals are separated from the  $d_{z^2}$  and  $d_{x^2-y^2}$  because of the crystal field. The main peaks at  $E - E_F \approx -3.5$  and  $\approx -1.2$  eV correspond to the bonding and anti-bonding states between the Cu and the Co  $d_{xy}$ ,  $d_{xz}$  and  $d_{yz}$  orbitals. In contrast, the low peak and the shoulder correspond to the bonding and anti-bonding states between the Co and the Cu  $d_{z^2}$  orbital along the transport direction, and the bonding and anti-bonding Co  $d_{x^2-y^2}$  band in the perpendicular direction. The Co-Cu bonding states have predominately Cu character, while the Co-Cu anti-bonding states near the Fermi energy have mostly Co character.

In the minority (spin down) channel, the DFT DOS presents two pronounced peaks at opposite sides of the Fermi energy, while features below  $E - E_F \approx -3$  eV are less marked than in the majority channel. The occupied peak at  $E - E_F \approx -0.8$  eV originates mostly from the Co  $d_{x^2-y^2}$ . In contrast, the unoccupied peak centered at  $E - E_F \approx 0.1$  eV bears contributions from the other four  $d$  orbitals. Overall, we estimate a splitting of the majority and minority  $d$  bands in the range between 1.1 and 1.5 eV, depending on the considered  $d$  orbital. Furthermore, we also note that the Co  $s$  band is also spin-polarized as a result of the hybridization with the  $d$  states.

In the DMFT calculations, the dynamical self-energy induces some redistribution of the spectral weight. The changes in the DOS are more pronounced for the majority than for minority channel. The main occupied

peak in the Co majority DOS is shifted towards the Fermi level, while the minority DOS is barely affected. As a result, the spin splitting of the  $d$  states is reduced compared to DFT. The orbital character of the main peaks is preserved, as it is dictated by the system symmetry and the crystal field. However, we observe a considerable spectral narrowing of the states close to the Fermi level, while the states below  $E - E_F \approx -3$  eV broaden and extend toward much lower energies. Overall, these changes are typical for correlation effects in transition metals, as discussed in a number of works (for example Refs.<sup>29,31,37,51</sup>), and can be understood by inspecting the many-body self-energy. This is shown for each Co  $d$  orbital in Fig. 6, where the real (imaginary) part is represented by the solid (dashed) line. The self-energies of the various orbitals present some differences, nonetheless we can point to some common features, which will also be important to understand the results for the transmission function. The self-energy near the Fermi level has Fermi-liquid character: the imaginary part goes to zero as  $-\text{Im}\Sigma_{MB}^{\sigma}(E) \propto (E - E_F)^2$ . Away from the Fermi energy, the self-energy is much larger for the majority than minority channel, indicating that majority electrons are more correlated than minority electrons. The absolute magnitude of  $\text{Im}\Sigma_{MB}^{\uparrow}$  is large in the energy range between  $E - E_F \approx -2$  eV and  $-5$  eV resulting in the large broadening of the DOS.  $\text{Re}\Sigma_{MB}^{\uparrow}(E)$  of the  $d_{xy}$ ,  $d_{yz}$ , and  $d_{xz}$  ( $d_{z^2}$  and  $d_{x^2-y^2}$ ) orbitals is positive at energies  $E - E_F \gtrsim -4.4$  ( $-2.9$ ) eV, and it shows a maximum at about  $E - E_F \approx -1.5$  eV. This causes the shift of the occupied majority  $d$  states towards the Fermi level as observed in Fig. 4. On the other hand, for energies  $E - E_F \lesssim -4.5$  eV, the real part of  $\Sigma_{MB}^{\uparrow}(E)$  is negative, and draws the majority spectral weight towards lower energies. In the minority down channel, the real part of  $\Sigma_{MB}^{\downarrow}(E)$  for the Co  $d_{x^2-y^2}$  orbital has a small peak at about  $E - E_F \approx -0.7$  eV, which shifts the orbital state towards the Fermi level by about 0.5 eV. The imaginary part of  $\Sigma_{MB}^{\downarrow}(E)$  of all orbitals is considerably smaller than that of  $\Sigma_{MB}^{\uparrow}(E)$  at high negative energies. However, it is larger in the energy regions just below and above the Fermi level.

The spin-dependent DFT and DMFT transmission  $T^{\sigma}(E)$ , calculated respectively using Eqs. (7) and Eq. (15), are presented in Fig. 7. In the DFT case,  $T^{\sigma}(E)$  is quite large ( $> 0.5$ ) over the whole displayed energy range because the system is an all-metallic heterostructure.  $T^{\sigma}(E)$  presents rather sharp peaks in the energy region below the Fermi level, where Co  $d$  states are located, whereas  $T^{\sigma}(E)$  is quite smooth above the Fermi energy, where  $s$  states dominate. In the DMFT calculations,  $T^{\sigma}(E)$  is drastically suppressed. This is because of two effects, which dominate at different energies. Firstly, the Co  $d$  states acquire a finite relaxation time  $\tau$ , which is reflected by the imaginary part of the many-body self-energy,  $\tau^{-1} \propto \text{Im}\Sigma_{MB}^{\sigma}$ . Secondly, the position in energy of the occupied Co  $d$  states is shifted towards

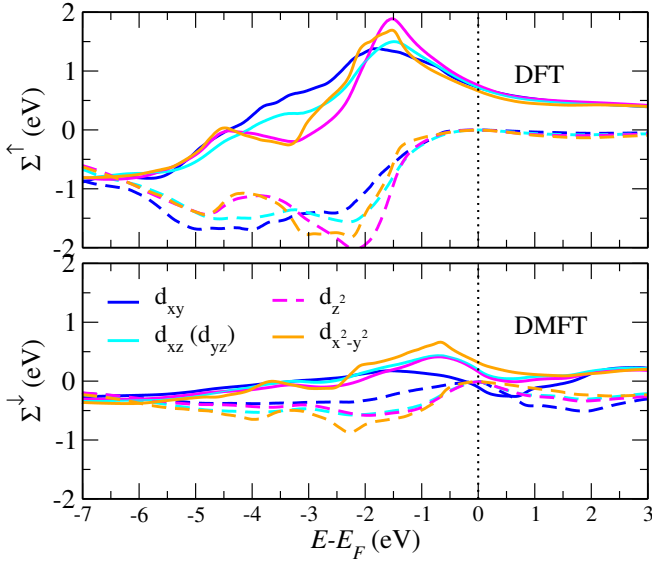


FIG. 6. Real part (solid line) and imaginary part (dashed line) of the many-body self-energy for each Co 3d orbital in the Cu/Co/Cu system. The upper panel is for majority (spin up), while the bottom panel is for minority (spin down) electrons.

Fermi level by the real part of the self-energy, and, as a result, the Cu  $s$  conduction electrons undergo a more pronounced elastic scattering at the Co layer. Focusing in particular on the majority spin channel (top panel of Fig. 7), DFT predicts the  $d$  states to contribute to the peaks in  $T^\uparrow(E)$  between  $E - E_F \approx -6$  and  $-1.3$  eV. In the DMFT calculations these peaks are suppressed, mostly because of the finite relaxation time. The imaginary part of the self-energy is in fact very large in that energy range. In contrast, at energies from  $E - E_F \approx -1.3$  eV to 1 eV, the DMFT majority transmission  $T^\uparrow(E)$  is reduced owing to the elastic scattering of the  $s$  states with the Co  $d$  orbitals, since  $\text{Im}\Sigma_{MB}^\uparrow(E) \approx 0$  and  $\text{Re}\Sigma_{MB}^\uparrow(E)$  is large. In the minority spin channel, the energy position of the  $d$  states is not drastically modified by DMFT (see the central panel of Fig. 7), since the effect of the real part of the self-energy is negligible. Hence, the suppression of the transmission  $T^\downarrow(E)$  in the energy ranges  $-1.8 \lesssim E - E_F < 0$  eV and  $0 < E - E_F \lesssim 2$  eV, where the  $d$  states spectral weight is the largest, is mostly due to the finite relaxation time. The transmission at the Fermi energy remains unaffected since  $\text{Im}\Sigma_{MB}^\downarrow(E_F) = 0$  and  $\text{Re}\Sigma_{MB}^\downarrow(E_F) \approx 0$ .

From the transmission function we can define the energy-dependent spin-polarization

$$SP(E) = \frac{T^\uparrow(E) - T^\downarrow(E)}{T^\uparrow(E) + T^\downarrow(E)}, \quad (40)$$

which is plotted in the bottom panel of Fig. 7. In the energy range from  $E - E_F \approx -4$  to 0 eV, DFT gives the largest  $SP$ . In contrast, DMFT predicts that  $SP$  changes sign and almost vanishes owing the

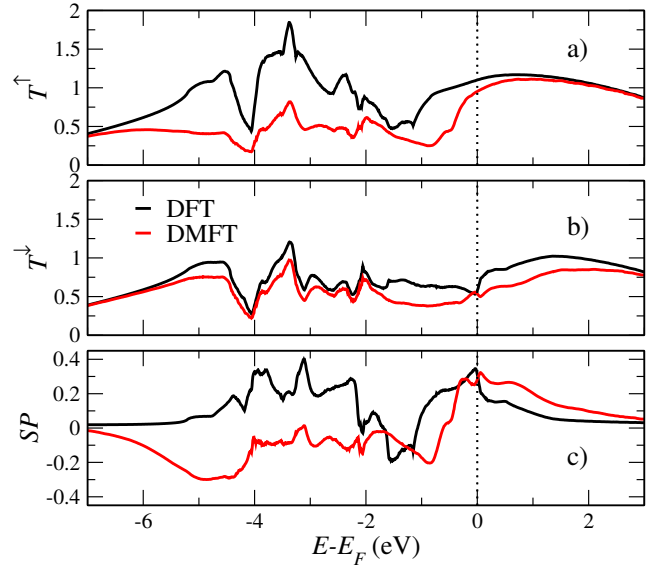


FIG. 7. (a) Transmission function as a function of energy for the Cu/Co/Cu system, for majority (spin up) electrons. (b) Transmission function as a function of energy for minority (spin down) electrons. (c) Spin-polarization as a function of energy. DFT (DMFT) results are in black (red).

suppression of the transmission for majority  $d$  electrons. However, at the Fermi energy the difference between the DFT and DMFT results is quite small, and we predict  $SP(E_F)$  respectively equal to 0.31 and 0.27. These very close values at  $E_F$  are due to the fact that the majority conduction electrons are mostly  $s$  states, while the minority transmission function is very similar in DFT and DMFT. Next we look at  $SP$  in the energy range above the Fermi level. Here the DMFT value is larger than the DFT one. This is because, as discussed above,  $T^\uparrow(E)$  is due only to uncorrelated  $s$  electrons, whereas  $T^\downarrow(E)$  has a contribution also from the minority  $d$  states, which acquire a finite relaxation time in DMFT, and whose transmission is therefore partially suppressed. The opposite situation is found instead for  $E - E_F \lesssim -4$ , where DMFT reduces drastically the majority transmission, but does not affect the minority one. As a result, the  $SP$  is negligible according to DFT calculations, but it is large and negative when including dynamical self-energy effects.

## B. Correlated Co multilayered device

We now consider a heterostructure, whose central region comprises two Co trilayers separated via a Cu spacer. We denote this structure as Cu/Co<sub>3</sub>/Cu<sub>3</sub>/Co<sub>3</sub>/Cu. This device, which is shown in Fig. 3, represents a spin-valve, where the magnetization of the Co trilayer on left side can be set parallel (P) or antiparallel (AP) to the magnetization of the Co trilayer

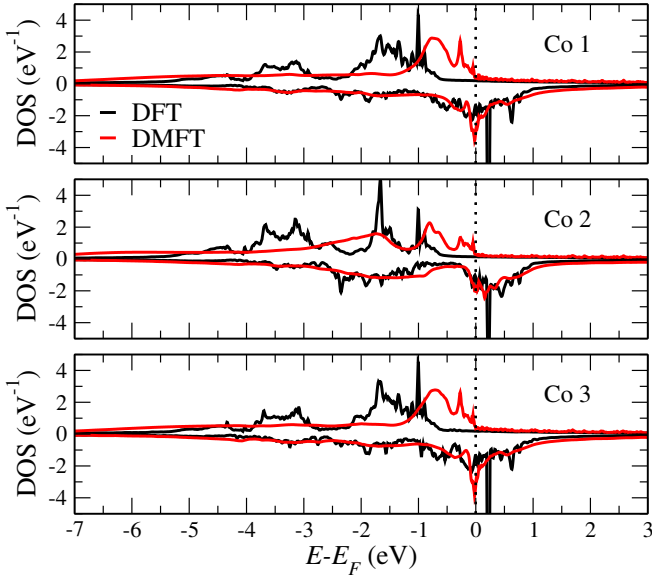


FIG. 8. DOS of the Co atoms in three different layers of the Cu/Co<sub>3</sub>/Cu<sub>3</sub>/Co<sub>3</sub>/Cu system, calculated with DFT and DMFT. The atoms Co 1, Co 2 and Co 3 are indicated in Fig. 3.

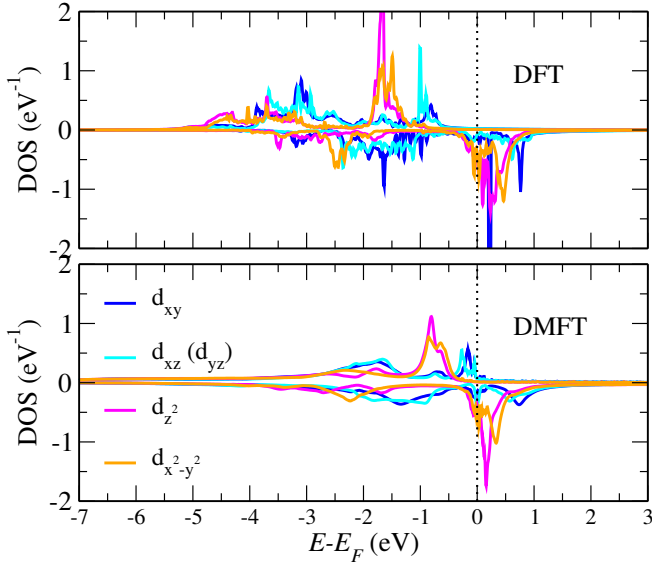


FIG. 9. DOS projected over the  $3d$  orbitals of the Co 2 atom in Cu/Co<sub>3</sub>/Cu<sub>3</sub>/Co<sub>3</sub>/Cu. Top panel: DFT calculation, Bottom panel: DMFT calculation.

on the right side of the central region.

The DOS of a Co trilayer is presented in Fig. 8. Co 1, 2 and 3 indicate the Co atoms in the three different layers (see Fig. 3). Co 1 and Co 3, which are at the interface with Cu, have almost identical electronic structure. Their DOS is very similar to that of the single Co layer, and the main features can be attributed to the different  $d$  orbitals as described in the previous section. In contrast, the DOS of Co 2, which is in the

middle of a trilayer, is significantly different. Co 2 forms bonding and anti-bonding states with the surrounding Co atoms. In the DFT calculations, the majority bonding and antibonding states extend over the energy regions  $-5 \lesssim E - E_F < -2.5$  eV and  $-1.8 \lesssim E - E_F < -0.5$  eV, respectively. The majority  $d$  states are therefore almost fully occupied. In the minority channel, the bonding states are located in energy between  $E - E_F \approx -2.5$  and  $-1$  eV, while the antibonding states cross the Fermi level. In the orbital-resolved DOS (Fig. 9), we note that the crystal field splitting for Co 2 is larger than for Co 1 and 3. Specifically, we find a separation of about 0.5 eV between the triplet states,  $d_{xy}$ ,  $d_{xz}$  and  $d_{yz}$ , and the doublet state,  $d_{x^2-y^2}$  and  $d_{z^2}$ . For all three different Co atoms, DMFT induces a redistribution of the DFT spectral weight for the majority channel and, therefore, reduces the  $d$  states exchange splitting. The self-energy is qualitatively similar to that discussed in the previous section for the Co monolayer. The orbital character of the different features in the DOS is preserved.

The transmission function  $T_P^\sigma(E)$  and  $T_{AP}^\sigma(E)$  for the P configuration and the AP configuration are shown in Fig. 10. We first analyze the P case. In the DFT calculations both  $T_P^\uparrow(E)$  and  $T_P^\downarrow(E)$  are qualitatively very similar to the transmission obtained for Cu/Co/Cu. Nonetheless, DMFT now almost completely suppresses the transmission through the Co  $d$  states. The DMFT  $T_P^\uparrow(E)$  becomes of the order of 0.01 in the energy region between  $E - E_F \approx -4.5$  eV and  $\approx -0.5$  eV, while it remained of as large as about 0.5 in Cu/Co/Cu. This effect can be ascribed to the presence of six Co layers instead of just one. In each of the layers electrons acquire a finite relaxation time due to the imaginary part of the self-energy. If there were more Co layers the transmission would further diminish. In contrast, for energies  $E - E_F \gtrsim -0.5$ , where the conduction is due to  $s$  electrons, the DMFT  $T_P^\uparrow(E)$  of Cu/Co<sub>3</sub>/Cu<sub>3</sub>/Co<sub>3</sub>/Cu remains similar to the majority transmission of Cu/Co/Cu. Similar results are also found for the minority channel. Our analysis shows that the use of DMFT allows to quantitatively compute the reduction of the coherent transmission due to electron relaxation. The incoherent contributions to the conductance are expected to become larger as the coherent transmission decreases with increasing number of Co layers. As outlined in Sec. II B, the inclusion of inelastic contributions to the non-equilibrium transport properties of complex systems directly in the NEGF formalism however remains an open issue. In spite of that, our method allows to obtain an estimate for the orbital dependent relaxation time as function of energy as the inverse of the imaginary part of the computed many-body self-energy. For thin film systems exhibiting Fermi liquid behaviour, such as the Co/Cu heterostructures investigated here, the imaginary part of the many-body self-energy vanishes at  $E_F$ . Hence, at zero bias the electron transport is expected to be dominated by the coherent contribution.

We now turn to analyze the spin-valve performance of Cu/Co<sub>3</sub>/Cu<sub>3</sub>/Co<sub>3</sub>/Cu. The total transmission of the

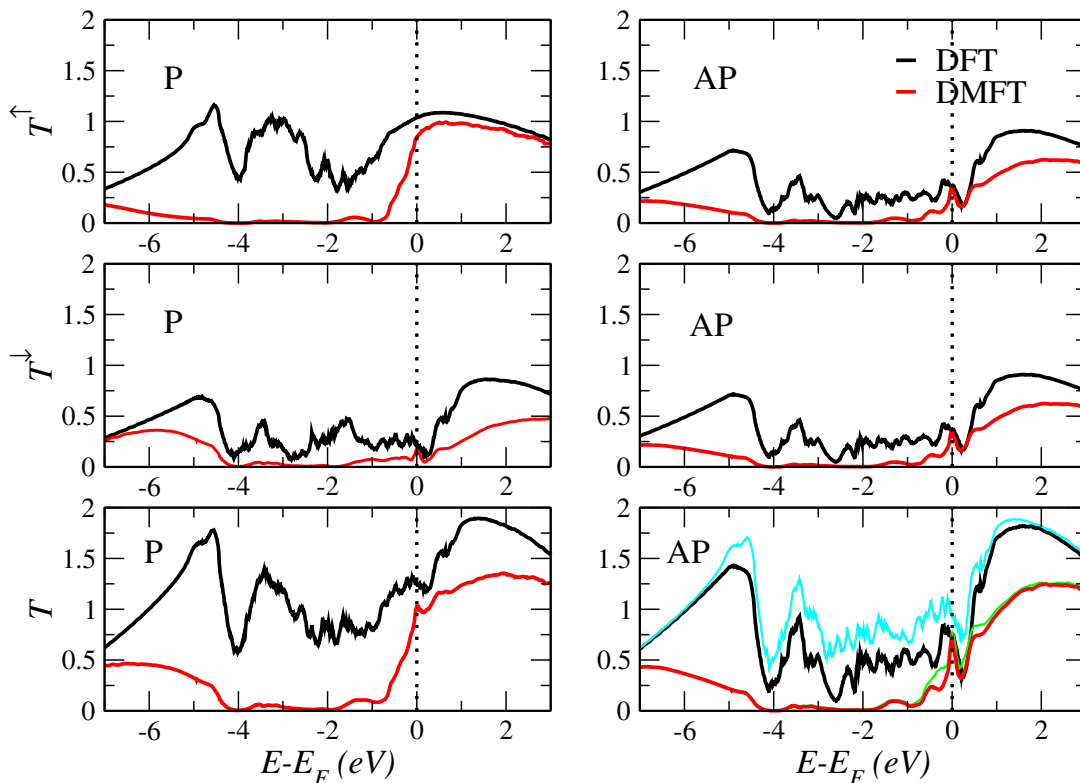


FIG. 10. Majority, minority and total transmission,  $T^\uparrow(E)$ ,  $T^\downarrow(E)$  and  $T(E) = T^\uparrow(E) + T^\downarrow(E)$ , for Cu/Co<sub>3</sub>/Cu<sub>3</sub>/Co<sub>3</sub>/Cu (left panels: P configuration; right panels: AP configuration). In the bottom right panel, the cyan (green) curve represents the AP transmission function calculated using the model approximation  $T_{AP}(E) \sim 2\sqrt{T_P^\uparrow(E)T_P^\downarrow(E)}$  using the DFT (DMFT)  $T_P^\uparrow(E)$  and  $T_P^\downarrow(E)$ .

parallel and antiparallel configurations are  $T_{P(AP)}(E) = T_{P(AP)}^\uparrow(E) + T_{P(AP)}^\downarrow(E)$ . The results are presented in the two bottom panels of Fig. 10. DFT predicts that  $T_P(E) \gg T_{AP}(E)$  over a wide energy region. In contrast, the difference between the P and AP transmission is much less marked in DMFT. By modelling the left Co/Cu and the right Cu/Co interfaces as two independent scatterers in series, we can use a phenomenological expression for the AP transmission  $T_{AP}(E) \sim 2\sqrt{T_P^\uparrow(E)T_P^\downarrow(E)}$  (Ref. 28). The resulting DFT and DMFT results are represented by the cyan and green lines in the bottom right panel of Fig. 10, respectively. The DMFT  $T_{AP}(E)$  is in very good agreement with this model, while for the DFT results the agreement is less good. This indicates that quantum interference effects are largely suppressed by DMFT.

To quantitatively characterize the spin transport properties of the system, we compute the zero-bias GMR:

$$GMR = \frac{T_P(E_F) - T_{AP}(E_F)}{T_{AP}(E_F)}. \quad (41)$$

DFT and DMFT calculations give  $GMR = 0.76$  and  $0.63$ , respectively. DMFT reduces the GMR by about 17% when compared to DFT. The transport at the Fermi

energy is mostly due to  $s$  electrons in the majority channels. These are not correlated, but DMFT predicts enhanced elastic scattering of  $s$  states with the  $d$  states, which are shifted closer to the Fermi energy than in DFT calculations. In the minority channel, there are mostly  $d$  states near the Fermi energy, but self-energy dynamical corrections are negligible. Hence  $T_P(E_F)$  is suppressed more than  $T_{AP}(E_F)$ , and we therefore get the reduced GMR. This is our main observation about the effect of electron correlations on spin transport, and, although it refers to a specific device, it is quite general at the qualitative level, and will also apply to more complex TM-based spin-valve structures.

## V. CONCLUSIONS

We presented a computational scheme using LSDA+DMFT to investigate the linear-response spin-dependent electron transport through nanoscale two-terminal devices. The method is implemented in the Smeagol code, and it can be interfaced with any DMFT impurity solver. For the results in this paper we used second-order perturbation theory for the impurity solver, which allowed to compute the Green's function

and self-energy directly for real energies, thus avoiding numerical problems due to the analytic continuation. Perturbation theory is only appropriate for moderately correlated systems, such as *3d* ferromagnetic TMs. With this solver the LSDA+DMFT transport calculations are only slightly more complicated and computational demanding than standard DFT+NEGF calculations, thereby making it an ideal tool for the wider user community.

We applied the developed LSDA+DMFT method to heterostructures comprising alternating Co and Cu layers. At energies away from  $E_F$  the coherent transmission in these systems is suppressed by electron correlations. This is due to the finite imaginary part of the many-body self-energy, which corresponds to the inverse of an effective electron lifetime. At  $E_F$ , due to the Fermi liquid behaviour, the imaginary part of the self-energy vanishes, so that the changes in the transmission are entirely determined by the DMFT-induced shift of the energy spectrum. For the Co/Cu heterostructures we find that the transport at the Fermi energy, and therefore the linear-response conductance, is mostly due to uncorrelated majority *s* electrons. DMFT predicts that they undergo enhanced elastic scattering with the Co *3d* states, since these are shifted when compared to

the DFT values. As a result, the GMR of spin-valve devices is reduced compared to DFT estimates. In the specific system studied here this reduction is of about 17%. Since the magnitude of the change in GMR is dictated by the DMFT-induced shifts of the electronic structure, in general arbitrarily large changes in GMR will be possible if the shift of peaks induced by DMFT is large.

## VI. ACKNOWLEDGEMENTS

AD acknowledges funding by the Science Foundation Ireland (SFI) and the Royal Society through the University Research Fellowship URF-R1-191769. MMR acknowledges funding provided by the Institute of Physics Belgrade, through the grant by the Ministry of Education, Science, and Technological Development of the Republic of Serbia. IR acknowledges the support of the UK government department for Business, Energy and Industrial Strategy through the UK national quantum technologies programme. LC acknowledges the financial support by the Deutsche Forschungsgemeinschaft through TRR80 (project F6) Project number 107745057. Computational resources were provided by Trinity College Dublin Research IT.

---

\* andrea.droghetti@tcd.ie

- <sup>1</sup> I. Žutić, J. Fabian, and S. Das Sarma, Rev. Mod. Phys. **76**, 323 (2004), URL <https://link.aps.org/doi/10.1103/RevModPhys.76.323>.
- <sup>2</sup> P. A. Grünberg, Rev. Mod. Phys. **80**, 1531 (2008), URL <https://link.aps.org/doi/10.1103/RevModPhys.80.1531>.
- <sup>3</sup> A. Fert, Rev. Mod. Phys. **80**, 1517 (2008), URL <https://link.aps.org/doi/10.1103/RevModPhys.80.1517>.
- <sup>4</sup> G. Binasch, P. Grünberg, F. Saurenbach, and W. Zinn, Phys. Rev. B **39**, 4828 (1989), URL <https://link.aps.org/doi/10.1103/PhysRevB.39.4828>.
- <sup>5</sup> M. N. Baibich, J. M. Broto, A. Fert, F. N. Van Dau, F. Petroff, P. Etienne, G. Creuzet, A. Friederich, and J. Chazelas, Phys. Rev. Lett. **61**, 2472 (1988), URL <https://link.aps.org/doi/10.1103/PhysRevLett.61.2472>.
- <sup>6</sup> J. Bass and W. Pratt, Journal of Magnetism and Magnetic Materials **200**, 274 (1999), ISSN 0304-8853, URL <https://www.sciencedirect.com/science/article/pii/S0304885399003169>.
- <sup>7</sup> R. Landauer, IBM Journal of Research and Development **1**, 223 (1957).
- <sup>8</sup> M. Büttiker, Phys. Rev. Lett. **57**, 1761 (1986), URL <https://link.aps.org/doi/10.1103/PhysRevLett.57.1761>.
- <sup>9</sup> M. Büttiker, IBM Journal of Research and Development **32**, 317 (1988).
- <sup>10</sup> E. Y. Tsymbal and D. G. Pettifor, Journal of Physics: Condensed Matter **9**, L411 (1997), URL <https://doi.org/10.1088/0953-8984/9/30/002>.

- <sup>11</sup> S. Sanvito, C. J. Lambert, J. H. Jefferson, and A. M. Bratkovsky, Phys. Rev. B **59**, 11936 (1999), URL <https://link.aps.org/doi/10.1103/PhysRevB.59.11936>.
- <sup>12</sup> R. O. Jones and O. Gunnarsson, Rev. Mod. Phys. **61**, 689 (1989), URL <http://link.aps.org/doi/10.1103/RevModPhys.61.689>.
- <sup>13</sup> W. Kohn, Rev. Mod. Phys. **71**, 1253 (1999).
- <sup>14</sup> R. O. Jones, Rev. Mod. Phys. **87**, 897 (2015), URL <http://link.aps.org/doi/10.1103/RevModPhys.87.897>.
- <sup>15</sup> U. von Barth and L. Hedin, J. Phys. C **5**, 1629 (1972).
- <sup>16</sup> S. H. Vosko, L. Wilk, and M. Nusair, Can. J. Phys. **58**, 1200 (1980).
- <sup>17</sup> J. P. Perdew, J. A. Chevary, S. H. Vosko, K. A. Jackson, M. R. Pederson, D. J. Singh, and C. Fiolhais, Phys. Rev. B **46**, 6671 (1992), URL <https://link.aps.org/doi/10.1103/PhysRevB.46.6671>.
- <sup>18</sup> J. P. Perdew, J. A. Chevary, S. H. Vosko, K. A. Jackson, M. R. Pederson, D. J. Singh, and C. Fiolhais, Phys. Rev. B **48**, 4978 (1993), URL <https://link.aps.org/doi/10.1103/PhysRevB.48.4978.2>.
- <sup>19</sup> J. P. Perdew, K. Burke, and M. Ernzerhof, Phys. Rev. Lett. **77**, 3865 (1996), URL <https://link.aps.org/doi/10.1103/PhysRevLett.77.3865>.
- <sup>20</sup> D. Wortmann, H. Ishida, and S. Blügel, Phys. Rev. B **65**, 165103 (2002), URL <https://link.aps.org/doi/10.1103/PhysRevB.65.165103>.
- <sup>21</sup> D. Wortmann, H. Ishida, and S. Blügel, Phys. Rev. B **66**, 075113 (2002), URL <https://link.aps.org/doi/10.1103/PhysRevB.66.075113>.
- <sup>22</sup> J. Kudrnovský, V. Drchal, C. Blaas, P. Weinberger, I. Turek, and P. Bruno, Phys. Rev. B

- 62**, 15084 (2000), URL <https://link.aps.org/doi/10.1103/PhysRevB.62.15084>.
- <sup>23</sup> J. M. MacLaren, X.-G. Zhang, W. H. Butler, and X. Wang, Phys. Rev. B **59**, 5470 (1999), URL <https://link.aps.org/doi/10.1103/PhysRevB.59.5470>.
- <sup>24</sup> P. A. Khomyakov, G. Brocks, V. Karpan, M. Zwierzycki, and P. J. Kelly, Phys. Rev. B **72**, 035450 (2005), URL <https://link.aps.org/doi/10.1103/PhysRevB.72.035450>.
- <sup>25</sup> J. Taylor, H. Guo, and J. Wang, Phys. Rev. B **63**, 245407 (2001), URL <https://link.aps.org/doi/10.1103/PhysRevB.63.245407>.
- <sup>26</sup> M. Brandbyge, J.-L. Mozos, P. Ordejón, J. Taylor, and K. Stokbro, Phys. Rev. B **65**, 165401 (2002), URL <https://link.aps.org/doi/10.1103/PhysRevB.65.165401>.
- <sup>27</sup> A. R. Rocha, V. M. García-Suárez, S. Bailey, C. Lambert, J. Ferrer, and S. Sanvito, Phys. Rev. B **73**, 085414 (2006), URL <https://link.aps.org/doi/10.1103/PhysRevB.73.085414>.
- <sup>28</sup> I. Rungger, A. Droghetti, and M. Stamenova, in *Handbook of Materials Modeling. Vol. 1 Methods: Theory and Modeling*, edited by S. Yip and W. W. Andreoni (Springer International Publishing, 2019).
- <sup>29</sup> A. I. Lichtenstein, M. I. Katsnelson, and G. Kotliar, Phys. Rev. Lett. **87**, 067205 (2001).
- <sup>30</sup> S. Monastera, F. Manghi, C. A. Rozzi, C. Arcangeli, E. Wetli, H.-J. Neff, T. Greber, and J. Osterwalder, Phys. Rev. Lett. **88**, 236402 (2002), URL <https://link.aps.org/doi/10.1103/PhysRevLett.88.236402>.
- <sup>31</sup> J. Braun, J. Minár, H. Ebert, M. I. Katsnelson, and A. I. Lichtenstein, Phys. Rev. Lett. **97**, 227601 (2006), URL <https://link.aps.org/doi/10.1103/PhysRevLett.97.227601>.
- <sup>32</sup> W. Metzner and D. Vollhardt, Phys. Rev. Lett. **62**, 324 (1989).
- <sup>33</sup> A. Georges, G. Kotliar, W. Krauth, and M. J. Rozenberg, Rev. Mod. Phys. **68**, 13 (1996).
- <sup>34</sup> G. Kotliar and D. Vollhardt, Phys. Today **57**, 53 (2004).
- <sup>35</sup> G. Kotliar, S. Y. Savrasov, K. Haule, V. S. Oudovenko, O. Parcollet, and C. A. Marianetti, Rev. Mod. Phys. **78**, 865 (2006).
- <sup>36</sup> K. Held, Adv. Phys. **56**, 829 (2007).
- <sup>37</sup> A. Grechnev, I. Di Marco, M. I. Katsnelson, A. I. Lichtenstein, J. M. Wills, and O. Eriksson, Phys. Rev. B **76**, 035107 (2007), URL <https://link.aps.org/doi/10.1103/PhysRevB.76.035107>.
- <sup>38</sup> F. Beuşeanu, C. Horea, E.-V. Macocian, T. Jurcuţ, L. Vitos, and L. Chioncel, Phys. Rev. B **83**, 125107 (2011), URL <https://link.aps.org/doi/10.1103/PhysRevB.83.125107>.
- <sup>39</sup> L. Chioncel, I. Leonov, H. Allmaier, F. Beuşeanu, E. Arrigoni, T. Jurcuţ, and W. Pötz, Phys. Rev. B **83**, 035307 (2011), URL <https://link.aps.org/doi/10.1103/PhysRevB.83.035307>.
- <sup>40</sup> A. Östlin, L. Vitos, and L. Chioncel, Phys. Rev. B **98**, 235135 (2018), URL <https://link.aps.org/doi/10.1103/PhysRevB.98.235135>.
- <sup>41</sup> I. Di Marco, A. Held, S. Keshavarz, Y. O. Kvashnin, and L. Chioncel, Phys. Rev. B **97**, 035105 (2018), URL <https://link.aps.org/doi/10.1103/PhysRevB.97.035105>.
- <sup>42</sup> S. Keshavarz, I. Di Marco, D. Thonig, L. Chioncel, O. Eriksson, and Y. O. Kvashnin, Phys. Rev. Materials **4**, 021401 (2020), URL <https://link.aps.org/doi/10.1103/PhysRevMaterials.4.021401>.
- <sup>43</sup> D. Jacob, K. Haule, and G. Kotliar, Phys. Rev. Lett. **103**, 016803 (2009), URL <https://link.aps.org/doi/10.1103/PhysRevLett.103.016803>.
- <sup>44</sup> D. Jacob, K. Haule, and G. Kotliar, Phys. Rev. B **82**, 195115 (2010), URL <https://link.aps.org/doi/10.1103/PhysRevB.82.195115>.
- <sup>45</sup> D. Jacob, Journal of Physics: Condensed Matter **27**, 245606 (2015), URL <https://doi.org/10.1088/0953-8984/27/24/245606>.
- <sup>46</sup> D. Jacob, M. Soriano, and J. J. Palacios, Phys. Rev. B **88**, 134417 (2013), URL <https://link.aps.org/doi/10.1103/PhysRevB.88.134417>.
- <sup>47</sup> A. Droghetti and I. Rungger, Phys. Rev. B **95**, 085131 (2017), URL <https://link.aps.org/doi/10.1103/PhysRevB.95.085131>.
- <sup>48</sup> W. H. Appelt, A. Droghetti, L. Chioncel, M. M. Radonjić, E. Muñoz, S. Kirchner, D. Vollhardt, and I. Rungger, Nanoscale **10**, 17738 (2018), URL <http://dx.doi.org/10.1039/C8NR03991G>.
- <sup>49</sup> D. Jacob, **30**, 354003 (2018), URL <https://doi.org/10.1088/1361-648x/aad523>.
- <sup>50</sup> M. Rumetshofer, D. Bauernfeind, E. Arrigoni, and W. von der Linden, Phys. Rev. B **99**, 045148 (2019), URL <https://link.aps.org/doi/10.1103/PhysRevB.99.045148>.
- <sup>51</sup> L. Chioncel, C. Morari, A. Östlin, W. H. Appelt, A. Droghetti, M. M. Radonjić, I. Rungger, L. Vitos, U. Eckern, and A. V. Postnikov, Phys. Rev. B **92**, 054431 (2015), URL <https://link.aps.org/doi/10.1103/PhysRevB.92.054431>.
- <sup>52</sup> C. Morari, W. H. Appelt, A. Östlin, A. Prinz-Zwick, U. Schwingenschlögl, U. Eckern, and L. Chioncel, Phys. Rev. B **96**, 205137 (2017), URL <https://link.aps.org/doi/10.1103/PhysRevB.96.205137>.
- <sup>53</sup> I. Rungger and S. Sanvito, Phys. Rev. B **78**, 035407 (2008), URL <https://link.aps.org/doi/10.1103/PhysRevB.78.035407>.
- <sup>54</sup> S. Okamoto and A. J. Millis, Phys. Rev. B **70**, 241104 (2004), URL <https://link.aps.org/doi/10.1103/PhysRevB.70.241104>.
- <sup>55</sup> M. Pothhoff and W. Nolting, Phys. Rev. B **59**, 2549 (1999), URL <https://link.aps.org/doi/10.1103/PhysRevB.59.2549>.
- <sup>56</sup> A. Weh, W. H. Appelt, A. Östlin, L. Chioncel, and U. Eckern, *physica status solidi (b)* **n/a**, 2100157 (????), <https://onlinelibrary.wiley.com/doi/pdf/10.1002/pssb.202100157>, URL <https://onlinelibrary.wiley.com/doi/abs/10.1002/pssb.202100157>.
- <sup>57</sup> S. Datta, *Electronic Transport in Mesoscopic Systems* (Cambridge University Press, Cambridge, UK, 1995).
- <sup>58</sup> J. M. Soler, E. Artacho, J. D. Gale, A. García, J. Junquera, P. Ordejón, and D. Sánchez-Portal, Journal of Physics: Condensed Matter **14**, 2745 (2002), URL <https://doi.org/10.1088/0953-8984/14/11/302>.
- <sup>59</sup> D. S. Fisher and P. A. Lee, Phys. Rev. B **23**, 6851 (1981), URL <https://link.aps.org/doi/10.1103/PhysRevB.23.6851>.
- <sup>60</sup> G. Stefanucci and R. van Leeuwen, *Nonequilibrium Many-Body Theory of Quantum Systems: A Modern Introduction* (Cambridge University Press, 2013).
- <sup>61</sup> A. Ferretti, A. Calzolari, R. Di Felice, F. Manghi, M. J. Caldas, M. B. Nardelli, and E. Molinari, Phys. Rev. Lett. **94**, 116802 (2005), URL <https://link.aps.org/doi/10.1103/PhysRevLett.94.116802>.

- <sup>62</sup> A. Ferretti, A. Calzolari, R. Di Felice, and F. Manghi, Phys. Rev. B **72**, 125114 (2005), URL <https://link.aps.org/doi/10.1103/PhysRevB.72.125114>.
- <sup>63</sup> K. S. Thygesen and A. Rubio, Phys. Rev. B **77**, 115333 (2008), URL <https://link.aps.org/doi/10.1103/PhysRevB.77.115333>.
- <sup>64</sup> Y. Meir and N. S. Wingreen, Phys. Rev. Lett. **68**, 2512 (1992), URL <https://link.aps.org/doi/10.1103/PhysRevLett.68.2512>.
- <sup>65</sup> H. Ness, L. K. Dash, and R. W. Godby, Phys. Rev. B **82**, 085426 (2010), URL <https://link.aps.org/doi/10.1103/PhysRevB.82.085426>.
- <sup>66</sup> H. Förster, P. Samuelsson, S. Pilgram, and M. Büttiker, Phys. Rev. B **75**, 035340 (2007), URL <https://link.aps.org/doi/10.1103/PhysRevB.75.035340>.
- <sup>67</sup> T.-K. Ng, Phys. Rev. Lett. **76**, 487 (1996), URL <https://link.aps.org/doi/10.1103/PhysRevLett.76.487>.
- <sup>68</sup> A. Oguri, Journal of the Physical Society of Japan **70**, 2666 (2001), <https://doi.org/10.1143/JPSJ.70.2666>, URL <https://doi.org/10.1143/JPSJ.70.2666>.
- <sup>69</sup> E. Pavarini, in *The LDA+DMFT approach to strongly correlated materials Modeling and Simulation Vol. 1*, edited by E. Pavarini, E. Koch, D. Vollhardt, and A. Lichtenstein (Forschungszentrum Jülich, 2011).
- <sup>70</sup> M. Karolak, G. Ulm, T. Wehling, V. Mazurenko, A. Poteryaev, and A. Lichtenstein, Journal of Electron Spectroscopy and Related Phenomena **181**, 11 (2010), ISSN 0368-2048, URL <https://www.sciencedirect.com/science/article/pii/S0368204810001222>.
- <sup>71</sup> K. Haule, C.-H. Yee, and K. Kim, Phys. Rev. B **81**, 195107 (2010), URL <https://link.aps.org/doi/10.1103/PhysRevB.81.195107>.
- <sup>72</sup> A. Valli, G. Sangiovanni, A. Toschi, and K. Held, Phys. Rev. B **86**, 115418 (2012), URL <https://link.aps.org/doi/10.1103/PhysRevB.86.115418>.
- <sup>73</sup> V. I. Anisimov, D. E. Kondakov, A. V. Kozhevnikov, I. A. Nekrasov, Z. V. Pchelkina, J. W. Allen, S.-K. Mo, H.-D. Kim, P. Metcalf, S. Suga, et al., Phys. Rev. B **71**, 125119 (2005), URL <https://link.aps.org/doi/10.1103/PhysRevB.71.125119>.
- <sup>74</sup> F. Lechermann, A. Georges, A. Poteryaev, S. Biermann, M. Posternak, A. Yamasaki, and O. K. Andersen, Phys. Rev. B **74**, 125120 (2006), URL <https://link.aps.org/doi/10.1103/PhysRevB.74.125120>.
- <sup>75</sup> B. Amadon, F. Lechermann, A. Georges, F. Jollet, T. O. Wehling, and A. I. Lichtenstein, Phys. Rev. B **77**, 205112 (2008), URL <https://link.aps.org/doi/10.1103/PhysRevB.77.205112>.
- <sup>76</sup> M. Aichhorn, L. Pourovskii, V. Vildosola, M. Ferrero, O. Parcollet, T. Miyake, A. Georges, and S. Biermann, Phys. Rev. B **80**, 085101 (2009), URL <https://link.aps.org/doi/10.1103/PhysRevB.80.085101>.
- <sup>77</sup> E. Plekhanov, P. Hasnip, V. Sacksteder, M. Probert, S. J. Clark, K. Refson, and C. Weber, Phys. Rev. B **98**, 075129 (2018), URL <https://link.aps.org/doi/10.1103/PhysRevB.98.075129>.
- <sup>78</sup> E. Gull, A. J. Millis, A. I. Lichtenstein, A. N. Rubtsov, M. Troyer, and P. Werner, Rev. Mod. Phys. **83**, 349 (2011), URL <https://link.aps.org/doi/10.1103/RevModPhys.83.349>.
- <sup>79</sup> A. I. Lichtenstein and M. I. Katsnelson, Phys. Rev. B **57**, 6884 (1998), URL <https://link.aps.org/doi/10.1103/PhysRevB.57.6884>.
- <sup>80</sup> M. I. Katsnelson and A. I. Lichtenstein, J. Phys.: Condens. Matter **11**, 1037 (1999).
- <sup>81</sup> M. I. Katsnelson and A. I. Lichtenstein, Eur. Phys. J. B **30**, 9 (2002).
- <sup>82</sup> L. V. Pourovskii, M. I. Katsnelson, and A. I. Lichtenstein, Phys. Rev. B **73**, 060506 (2006), URL <https://link.aps.org/doi/10.1103/PhysRevB.73.060506>.
- <sup>83</sup> M. Jarrell and J. Gubernatis, Physics Reports **269**, 133 (1996), ISSN 0370-1573, URL <https://www.sciencedirect.com/science/article/pii/0370157395000747>.
- <sup>84</sup> A. W. Sandvik, Phys. Rev. B **57**, 10287 (1998), URL <https://link.aps.org/doi/10.1103/PhysRevB.57.10287>.
- <sup>85</sup> A. S. Mishchenko, N. V. Prokof'ev, A. Sakamoto, and B. V. Svistunov, Phys. Rev. B **62**, 6317 (2000), URL <https://link.aps.org/doi/10.1103/PhysRevB.62.6317>.
- <sup>86</sup> S. Fuchs, T. Pruschke, and M. Jarrell, Phys. Rev. E **81**, 056701 (2010), URL <https://link.aps.org/doi/10.1103/PhysRevE.81.056701>.
- <sup>87</sup> J. W. Serene and D. W. Hess, Phys. Rev. B **44**, 3391 (1991), URL <https://link.aps.org/doi/10.1103/PhysRevB.44.3391>.
- <sup>88</sup> V. Drchal, V. Janiš, and J. Kudrnovský, Phys. Rev. B **60**, 15664 (1999), URL <https://link.aps.org/doi/10.1103/PhysRevB.60.15664>.
- <sup>89</sup> A. Droghetti, M. Radonjić, A. Halder, I. Rungger, and L. Chioncel, arXiv:2110.05883 (????), URL <https://arxiv.org/abs/2110.05883>.
- <sup>90</sup> A. A. Aligia, Phys. Rev. B **74**, 155125 (2006), URL <https://link.aps.org/doi/10.1103/PhysRevB.74.155125>.
- <sup>91</sup> N. Grewe and H. Keiter, Phys. Rev. B **24**, 4420 (1981), URL <https://link.aps.org/doi/10.1103/PhysRevB.24.4420>.
- <sup>92</sup> P. Coleman, Phys. Rev. B **29**, 3035 (1984), URL <https://link.aps.org/doi/10.1103/PhysRevB.29.3035>.
- <sup>93</sup> K. Haule, S. Kirchner, J. Kroha, and P. Wölfle, Phys. Rev. B **64**, 155111 (2001), URL <https://link.aps.org/doi/10.1103/PhysRevB.64.155111>.
- <sup>94</sup> T. Pruschke and N. Grewe, Z. Physik B - Condensed Matter **74**, 439 (1989), URL <https://doi.org/10.1007/BF01311391>.
- <sup>95</sup> A. Droghetti and R. I., unpublished (????).
- <sup>96</sup> M. Imada, A. Fujimori, and Y. Tokura, Rev. Mod. Phys. **70**, 1039 (1998).
- <sup>97</sup> V. I. Anisimov and O. Gunnarsson, Phys. Rev. B **43**, 7570 (1991), URL <https://link.aps.org/doi/10.1103/PhysRevB.43.7570>.
- <sup>98</sup> O. K. Andersen and T. Saha-Dasgupta, Phys. Rev. B **62**, R16219 (2000), URL <https://link.aps.org/doi/10.1103/PhysRevB.62.R16219>.
- <sup>99</sup> L. Vitos, Phys. Rev. B **64**, 014107 (2001), URL <https://link.aps.org/doi/10.1103/PhysRevB.64.014107>.
- <sup>100</sup> L. Vitos, H. Skriver, B. Johansson, and J. Kollár, Computational Materials Science **18**, 24 (2000), ISSN 0927-0256, URL <https://www.sciencedirect.com/science/article/pii/S0927025699000981>.
- <sup>101</sup> L. Chioncel, L. Vitos, I. A. Abrikosov, J. Kollár, M. I. Katsnelson, and A. I. Lichtenstein, Phys. Rev. B **67**, 235106 (2003), URL <https://link.aps.org/doi/10.1103/PhysRevB.67.235106>.